ACS OMEGA

http://pubs.acs.org/journal/acsodf

Article

Functionalized Magnetic Nanoparticles for NIR-Induced Photothermal Therapy of Potential Application in Cervical Cancer

Linxue Zhang,[#] Gulinigaer Alimu,[#] Zhong Du, Ting Yan, Hui Li, Rong Ma, Zhongwen Lan, Zhong Yu, Nuernisha Alifu,* and Ke Sun*

Cite This: *ACS Omega* 2023, 8, 21793−21801

Read Online

ACCESS | Metrics & More | Article Recommendations | Supporting Information

ABSTRACT: Photothermal therapy (PTT) holds great promise for cancer treatment with its effective ablation of solid tumors. As the essential core point, photothermal agents (PTAs) with excellent photothermal properties and good biocompatibility could help to fulfill highly efficient PTT. Herein, a novel type of nanoplatform Fe_3O_4@PDA/ICG (FPI) nanoparticle (NP) was designed and synthesized, which was composed of magnetic Fe_3O_4 and near-infrared excitable indocyanine green via encapsulation of polydopamine. The FPI NPs showed spherical structures in shape with uniform distribution and good chemical stability. Under 793 nm laser irradiation, FPI NPs could generate hyperthermia of 54.1 °C and photothermal conversion efficiency of 35.21%. The low cytotoxicity of FPI NPs was further evaluated and confirmed on HeLa cells with a high survival rate (90%). Moreover, under laser irradiation (793 nm), FPI NPs showed effective photothermal therapeutic characteristics for HeLa cells. Therefore, FPI NPs, as one of the promising PTAs, have great potential in the field of PTT for tumor treatment.

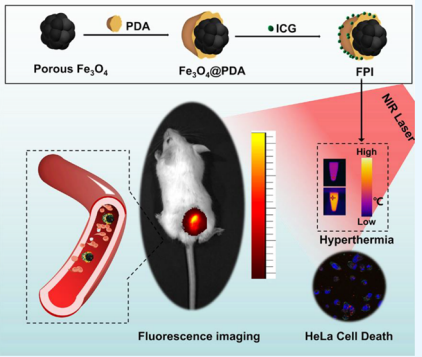

INTRODUCTION

To date, cervical cancer is the fourth most common gynecologic cancer, leading to a high probability of female death.[1−3] Although conventional strategies (including surgical resection, chemotherapy, and radiotherapy) are being utilized commonly in clinical practice for cervical cancer, their side effects are still unavoidable.[4] With a high therapeutic efficacy and appealing modality, photothermal therapy (PTT) has attracted widespread interest in cancer treatment.[5−7]

PTT is based on photothermal agents (PTAs) generating thermal effects under reasonable laser irradiation.[8−11] Notably, this is effective when the excitation light is in the near-infrared (NIR, 700−1700 nm) spectral region, which possesses deep tissue penetration and low scattering ability, resulting in the ablation of tumors with high efficiency.[12−14] Therefore, novel PTA nanoplatforms are urgently needed for efficacious cancer treatment. Among the existing PTAs, iron oxide (Fe_3O_4) is promising for the advantages of good magnetic properties, excellent photo-absorbing ability, and low toxicity.[15,16] Furthermore, Fe_3O_4 possesses the ability in MR imaging.[17] To obtain highly efficient and multi-modal treatment, much effort has been devoted to developing multifunctional PTAs based on Fe_3O_4.[18−22]

Polydopamine (PDA), one of the promising PTAs, possesses high photothermal conversion efficiency, biocompatibility, and biodegradability.[23−25] Notably, PDA could spontaneously convert into a universal coating polymer via an oxidative self-polymerization process under a moderate alkaline pH condition.[26−28] Thus, it is attractive to design multifunctional NPs by utilizing the PDA as the coating shell. Additionally, to make the multifunctional NPs "visible", indocyanine green (ICG) is a favorable one which has effective fluorescence intensity.[29−31] Furthermore, ICG could be excited by NIR light with low energy to produce heat.[32−34]

In this study, we designed and synthesized the multifunctional Fe_3O_4@PDA/ICG NPs (FPI NPs) based on magnetic Fe_3O_4 and NIR excitable/emissive clinical ICG via PDA. The FPI nanocomposite exhibited promising dispersion properties and chemical stability. In addition, the results of cytotoxicity assessment in HeLa cells further confirmed the low cytotoxicity of FPI NPs without laser irradiation. Under 793 nm laser excitation (power density: 0.33 W/cm^2), the FPI NPs converted NIR light into heat energy with a high temperature of 54.1 °C in 10 min. Furthermore, the photothermal conversion efficiency of FPI NPs was measured to be 35.21%. Then, FPI NPs exhibited a desirable therapeutic ability to vanquish cancer cells with highly efficient PTT during 793 nm laser irradiation. The photothermal stability of FPI NPs was verified through photothermal heating curves with heating and cooling experiments. Furthermore, the cellular uptake of FPI NPs (40 μg/mL) was performed by

Received: March 1, 2023
Accepted: May 30, 2023
Published: June 8, 2023

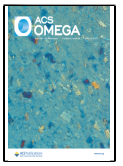

confocal laser scanning microscopy (CLSM), which showed a good anti-tumor effect. FPI NPs as photothermal materials provide great potential and a good alternative approach for antitumor PTT.

EXPERIMENTAL SECTION

Preparation of FP (Fe_3O_4@PDA NPs). Porous Fe_3O_4 NPs were synthesized through a traditional one-pot solvothermal route.[35] 1 mg of Fe_3O_4 NPs was dispersed into the volume of 3 mL of tris buffer (pH = 8.5) solution. Subsequently, 1 mg of PDA was dissolved in the above solution. The mixture was reacted at room temperature for 1 day under stirring. Finally, the Fe_3O_4@PDA NPs were washed several times with DI water to remove unreacted reagents and collected Fe_3O_4@PDA NPs.

Preparation of FPI (Fe_3O_4@PDA/ICG) NPs. According to previous work,[36] the content of 0.5 mg ICG was introduced into 1.5 mL of tris buffer (pH = 8.5. Then, the above solutions were added to Fe_3O_4@PDA NPs dispersion (1.5 mL) under mechanical stirring for 12 h. Afterward, the reactants were washed multiple times with DI water, and then FPI NPs products were collected.

Stability of FPI NPs. For the analysis of stability, the 100 μg/mL of FPI NPs was obtained from 100 μg of FPI NPs resuspended in DI water, and the absorption was further measured at pre-set time points (0, 12, 24, and 36 h).

Photothermal Effect and Performance. The photothermal properties of FPI NPs were assessed. The FPI NPs were exposed to an NIR laser (793 nm, 0.33 W/cm^2). Following exposure, an infrared thermometer monitored the changes in temperature from the sample in real-time. Briefly, the FPI NPs in aqueous dispersion at various concentrations (20, 40, 60, 80, and 100 μg/mL, respectively) with a volume of 500 μL were irradiated by an NIR laser of 793 nm for 10 min. In contrast, the temperature of the DI water, Fe_3O_4 in an aqueous dispersion and ICG in an aqueous solution were observed under the same continuous NIR laser irradiation for 10 min.

To examine the related performance of FPI NPs, including photostability and photothermal conversion efficiency (η), 0.05 mg of FPI NPs were distributed in 500 μL of water solutions and irradiated under 793 nm laser. The temperature of the samples was up to 54 °C. The FPI NPs suspension was cooled to room temperature after the 793 nm laser was switched off. The above process was repeated for five cycles, and the temperature change was monitored with an infrared camera. In contrast, we used the same condition to observe 1 mL of Fe_3O_4 in aqueous dispersion. According to the eq 1 as below, the η values[37,38] for Fe_3O_4 and FPI NPs were calculated:

$$\eta(\%) = \frac{hS(T_{max} - T_{sur})}{I(1 - 10^{-A_{793}})} \quad (1)$$

The $(T_{max} - T_{surr})$ was the result of maximum temperature after laser radiation minus room temperature. The I was the laser power density, and the value was equal to 0.33 W/cm^2, and A_{793} was the absorbance value of the sample at 793 nm. The h and S represented the heat transfer coefficients and the container's surface area, respectively. Furthermore, the value of hS could be acquired from eq 2:

$$hS = \frac{M_D C_D}{\tau_S} \quad (2)$$

The value of M_D (the mass of solvent) was 0.5 mg, and C_D (heat capacity of solvent) was 4.2 J/(g × °C), respectively. The τ_s was the constant of the sample system and value calculated by eq 3:

$$\tau_s = -\ln\left(\frac{T_t - T_{sur}}{T_{max} - T_{sur}}\right) \times 100\% \quad (3)$$

Cytotoxicity Analysis. HeLa cells were used to evaluate the cytotoxicity of FPI NPs. Briefly, the cells were inoculated in 96-well plates overnight in an incubator at 37 °C and 5% CO_2 with a density of 5 × 10^3 per well for overnight. The cytotoxicity of the material was assayed using the standard CCK-8 method. The cells were then incubated with various concentrations of Fe_3O_4 (0−100 μg/mL) and FPI NPs (0−100 μg/mL) for 8 h. Following incubation, the CCK-8 reagent (10 μL) was incubated with the cells of each well for 2 h. Each well's optical density (OD) was tested at the wavelength of 450 nm with an enzyme meter. Furthermore, cell viability was calculated as below eq 4:[39]

$$\text{cell viability}(\%) = \frac{(OD_{Sample} - OD_{Blank})}{(OD_{Negative\ control} - OD_{Blank})} \times 100\% \quad (4)$$

The cytotoxicity of FPI NPs was further analyzed. HeLa cells were treated with plates (1 × 10^5 cells/holes). The DMEM (control), DMEM + Laser, Fe_3O_4, and FPI NPs were incubated in HeLa cells for 8 h, then treated with 793 nm laser (0.33 W/cm^2) for 10 min. The Annexin V-FITC/PI Apoptosis Detection Kits were used to dyed with cells and the results were recorded.

Cell Uptake. CLSM (Nikon C2+, Japan) was utilized to analyze the cellular uptake of samples. HeLa cells in the logarithmic growth phase were inoculated with a volume of 600 μL and a density of 2.5 × 10^6 cells in confocal culture dishes and put in a 5% CO_2, temperature 37 °C incubator for 1 day. The cells were washed three times with 1 × PBS, followed by the treatment with 500 μL of complete culture containing Fe_3O_4 and FPI NPs (40 μg/mL) for 4 h. Then, the supernatant was discarded and washed three times with 1 × PBS, followed by the addition of 500 μL of Hoechst 33342 dye solution (1:100) for 20 min. The above cells were washed three times with 1 × PBS, and each culture dish was filled with fresh complete culture medium containing a volume of 600 μL. Furthermore, the fluorescence imaging was performed immediately with CLSM.

In Vitro Evaluation of PTT Effects. The procedure for culturing HeLa cells is the same as the above process. The cells were washed with 1 × PBS three times and then treated with 500 μL of complete medium containing Fe_3O_4 and FPI NPs (40 μg/mL) for 4 h. The supernatant was then discarded and washed three times with 1 × PBS, followed by the incubation of cells with 500 μL of Hoechst 33342 dye solution (1:100) and 500 μL of FITC dye solution (1:100) for 20 and 10 min, respectively. Cells were added with 500 μL of a fresh complete medium in each culture dish. Cells were then irradiated with a 793 nm continuous laser with the power of 0.33 W/cm^2 for 10 min in each well. The above irradiation procedure was performed at room temperature, and samples were imaged by CLSM immediately after being handled.

In Vivo PTT Effect and Fluorescence Property. Two groups of mice were used (n = 3 for each group). The control group 1 (injected with 200 μL PBS), while the mice group 2

https://doi.org/10.1021/acsomega.3c01374
ACS Omega 2023, 8, 21793−21801

were subcutaneously injected with FPI NPs (500 μg/mL, 200 μL). Under 793 nm NIR light irradiation, the mice were irradiated for 10 min. The temperature changes were recorded using an infrared camera. The fluorescence property of FPI NPs in mice was recorded by using an in vivo fluorescence imaging system (745 nm laser excitation and 840 nm emission). The control group 1 (injected with 200 μL PBS), the mice group 2 were subcutaneously injected with FPI NPs (500 μg/mL, 200 μL). Then, in vivo fluorescence analysis in the different group of mice was recorded after 2 h of injection.

RESULTS AND DISCUSSION

Synthesis and Characterization. Scheme 1 exhibits the synthesis process of Fe_3O_4@PDA/ICG (FPI) NPs. Under alkaline conditions, the polymerization of dopamine hydrochloride into PDA,[40] combined with magnetic Fe_3O_4 to construct Fe_3O_4@PDA. In tris buffer (pH = 8.5), ICG with good photothermal conversion performance connected to Fe_3O_4@PDA to form FPI NPs. The structure and morphology of the Fe_3O_4 and FPI NPs are shown in Figure 1. As observed, the uniformly Fe_3O_4 NPs showed a porous spherical shape and exhibited good aqueous dispersibility (Figure 1A,B). The surface area for the porous shape of nanoparticles can be tested according to the previous work.[41] Moreover, the M_s (saturation magnetization) of magnetic FPI NPs is 55.7 emu/g (Figure S1B). In addition, the MR effect of FPI NPs was tested by T_2-weighted MR imaging, as shown in Figure S1A. With increasing concentration of FPI NPs, the FPI NPs solution became darker. The magnet-responsive signal suggested its potential for MR imaging.[42] Figure 1C displays the XRD patterns of Fe_3O_4 NPs, which processed the peaks relating to the characteristic of face-centered cubic (FCC) structure for Fe_3O_4 (JCPDS 00-019-0629).

No other impurity peaks were found in the XRD pattern of Fe_3O_4 NPs, which indicated that the synthesized sample had a high purity. Then, to improve the biochemical properties and enhance the PTT efficiency, Fe_3O_4 NPs were further modified by ICG and PDA. The surface of FPI NPs encapsulated a transparent structure under transmitted electron beams which directly indicated the successful formation of the FPI NPs (Figure 1D,E). Furthermore, relevant UV−vis absorption spectroscopy was performed for the samples to further confirm the successful construction of the stable FPI NPs. Compared with Fe_3O_4 NPs and FP NPs (Figure S2A black and red line), UV−vis spectra of FPI NPs (Figure S2A blue line) showed strong absorption peaks around 785 nm, which was attributed to the existing ICG. According to previous related work on ICG,[43] the characteristic peak of ICG was measured at about 790 nm. Under the NIR light excitation, FPI NPs showed a suitable alternative for PTT as PTAs. Notably, the FPI NPs efficiently absorbed light in the NIR range of the spectrum and converted it to heat energy to ablate tumors. Furthermore, the positive zeta potential of Fe_3O_4 and FP NPs were measured to be 0.41 ± 0.04 and −3.6 ± 0.6 mV, respectively. After modification of ICG and PDA, FPI NPs kept a negative zeta

Scheme 1. NIR-Emissive FPI NPs for Target-Assisted PTT for Cervical Cancer

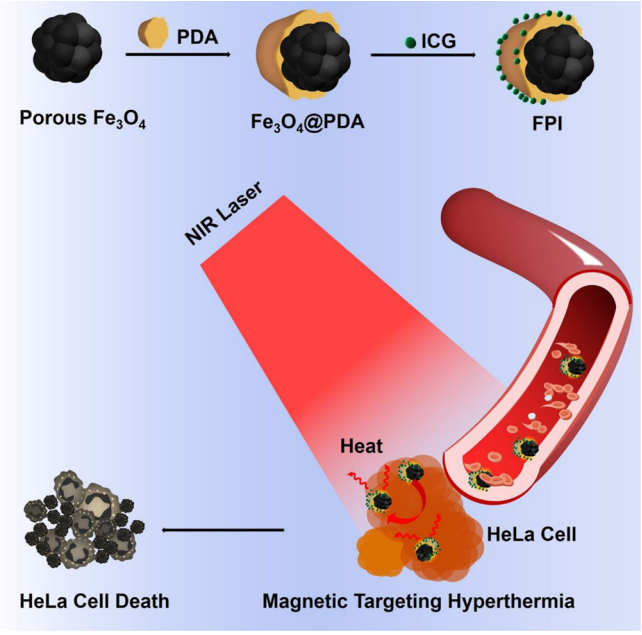

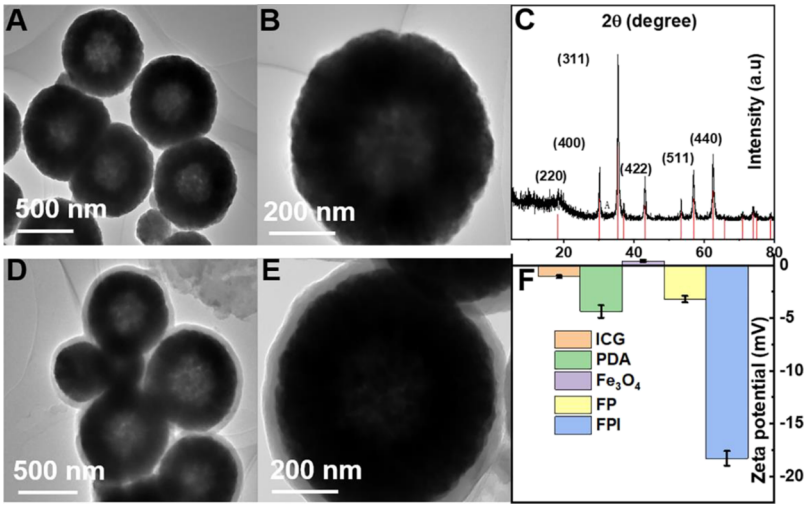

Figure 1. Morphology image of (A), (B) Fe_3O_4 structure, (C) XRD patterns of Fe_3O_4 NPs, morphology image of (D), (E) FPI structures. (F) Zeta potential of ICG, PDA, Fe_3O_4, FP, and FPI NPs.

https://doi.org/10.1021/acsomega.3c01374
ACS Omega 2023, 8, 21793−21801

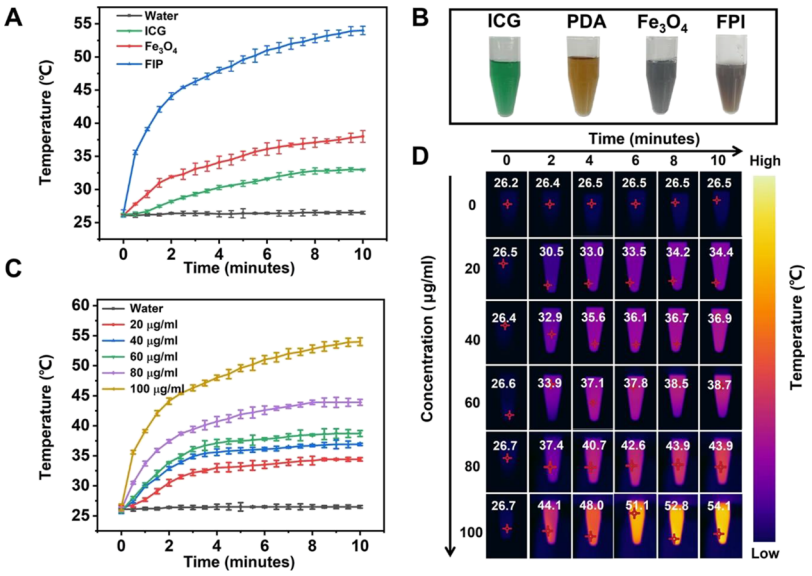

Figure 2. Photothermal performance of samples under 793 nm laser irradiation at a power density of 0.33 W/cm^2: (A) Temperature curves of ICG, Fe_3O_4, and FPI NPs in the aqueous dispersion (100 μg/mL) at various time points, respectively; (B) images of ICG, PDA, Fe_3O_4, and FPI NPs in the aqueous dispersion (from left to right, respectively); (C) temperature curves of FPI NP dispersions with various concentrations (20, 40, 60, 80, and 100 μg/mL); (D) NIR-thermal images for FPI NPs of different concentrations (20, 40, 60, 80, and 100 μg/mL).

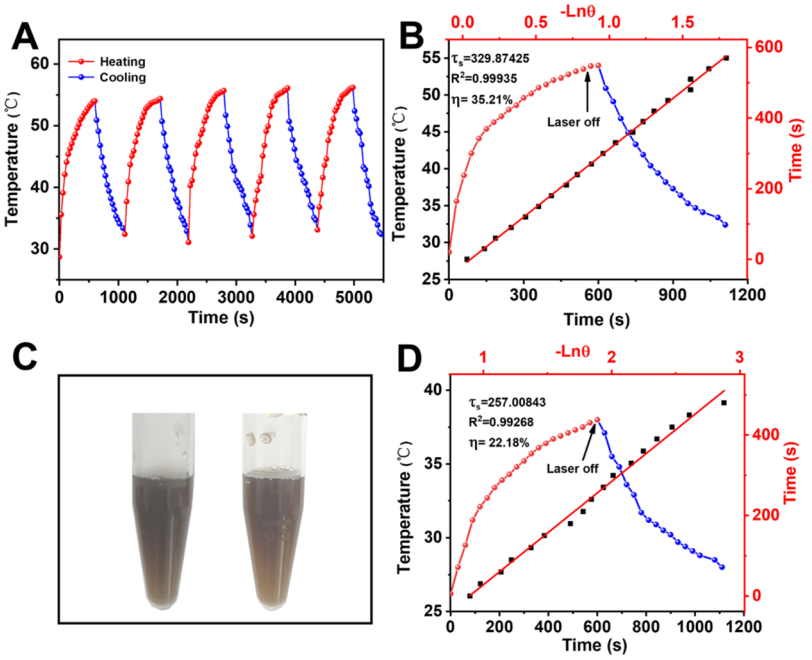

Figure 3. (A) Photothermal stability of FPI NPs (100 μg/mL) during five cycles with/without laser (793 nm, 0.33 W/cm^2). (B) Temperature evaluation of FPI NPs (100 μg/mL) with/without laser (793 nm, 0.33 W/cm^2), and linear time versus -Lnθ data of FPI NPs (during the cooling period). (C) Images of FPI NPs before (left)/after (right) laser (100 μg/mL, 793 nm, and 0.33 W/cm^2). (D) Temperature evaluation of free Fe_3O_4 (100 μg/mL) with/without laser (793 nm, 0.33 W/cm^2), and linear time versus -Lnθ data of free Fe_3O_4 (during the cooling period).

potential of 18.3 ± 1.1 mV. Therefore, these results indicate that ICG, PDA, and Fe_3O_4 NPs were successfully combined to construct FPI nanocomposite.

Stability of FPI NPs. The stability of FPI NPs was explored at different time points. The FPI NPs solution (100 μg/mL) was measured for the absorption and hydrodynamic size at different time points (0, 12, 24, and 36 h). In this study, the characteristic absorption spectra of FPI NPs at 785 nm display a negligible change (Figure S3A) in the long term and there is little difference change in FPI NPs size after a long term (Figure S3B).

Evaluation of Photothermal Effect. To verify the potential application of FPI NPs in PTT, the photothermal properties were explored for FPI NPs (500 μL, 100 mg/mL) in an aqueous dispersion under NIR laser irradiation (793 nm, 0.33 W/cm^2) for 10 min. Simultaneously under similar experimental conditions, the photothermal properties of Fe_3O_4 NPs and ICG NPs were further measured (Figure 2A). The images of an aqueous solution of ICG, Fe_3O_4, and

https://doi.org/10.1021/acsomega.3c01374
ACS Omega 2023, 8, 21793−21801

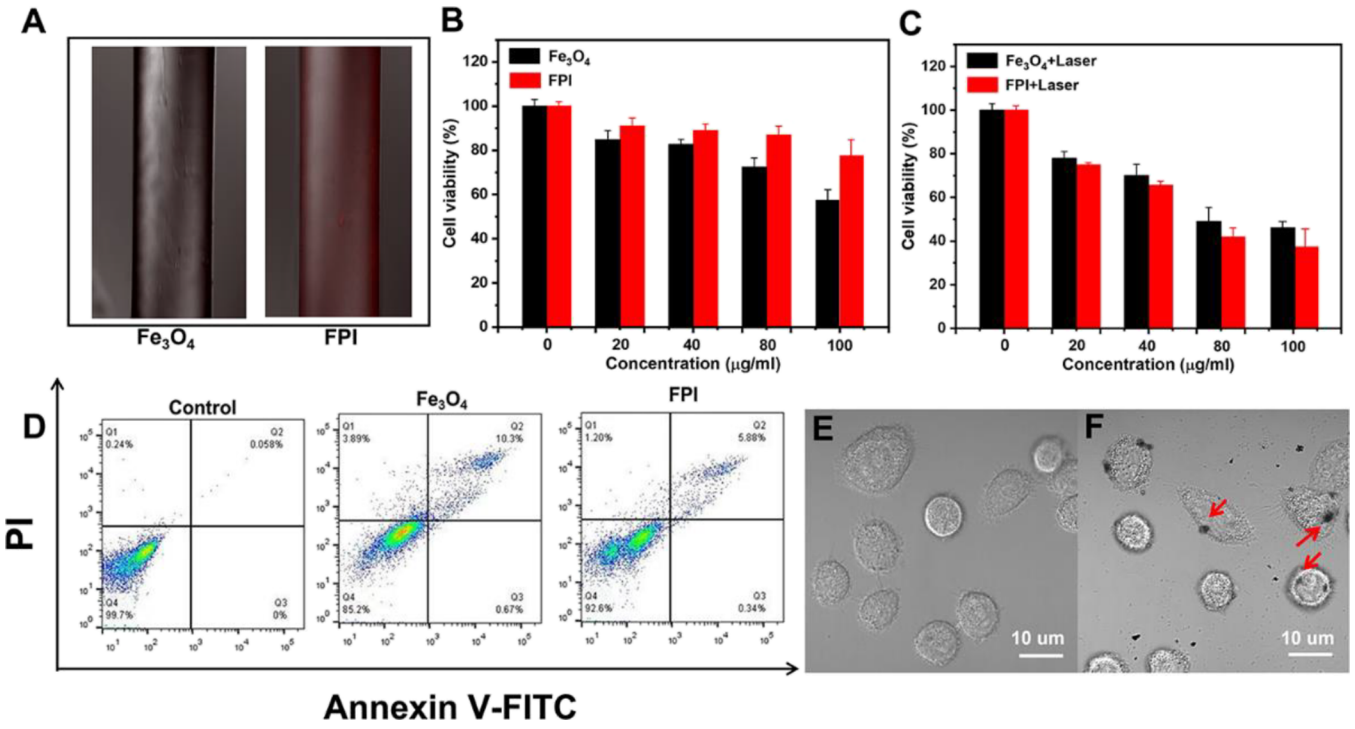

Figure 4. (A) Fluorescence image of Fe_3O_4 and FPI NPs (concentration of 100 mg/mL) under the CLSM (λ_{em} = 800−1000 nm, λ_{ex} = 640 nm). (B) HeLa cell cytotoxicity viability by CCK-8 of HeLa cells after incubation with Fe_3O_4 and FPI NPs at different concentrations (0, 20, 40, 80, and 100 μg/mL); (C) HeLa cell viability of Fe_3O_4 and FPI NPs at different concentrations (0, 20, 40, 80, and 100 μg/mL), assessed on treated cells that were laser-irradiated at 0.33 W/cm^2 for 10 min. (D) Flow cytometry in the case of Control, Fe_3O_4 (40 μg/mL), and FPI NPs (40 μg/mL). Confocal microscopy of cells in bright field (E) HeLa cell (control), (F) after HeLa cell treatment with FPI NPs for 4 h.

FPI NPs are shown in Figure 2B, which demonstrated good water solubility. Under the laser irradiation, the temperature of the water in the control group remained almost constant.

In contrast, the maximum temperature of FPI NPs could reach 54.1 °C, which suggested the photothermal properties of FPI NPs were much higher than Fe_3O_4 NPs, ICG NPs, or PDA[9] alone. Under the same laser irradiation, an obviously higher temperature elevation of FPI NPs reached 28.4 °C, owing to the PDA nanoshell process and the photothermal conversion property. Moreover, the existence of ICG could also produce a remarkable photothermal response under irradiation.[44]

Furthermore, the photothermal property of different concentrations of FPI NPs (20, 40, 60, 80, and 100 μg/mL) was explored under NIR laser irradiation with the power density of 0.33 W/cm^2, as shown in Figure 2C. As the concentration of FPI NPs increased, the maximum temperature of FPI NPs also increased. The results exhibited that the photothermal effect of FPI NPs dependent on the concentration of the samples. Under NIR laser radiation (0.33 W/cm^2), the jump temperature ΔT ($T_{max} - T_{surr}$) was larger than 13 °C when the FPI NPs at the concentration of 60, 80, and 100. Notably, the result was suitable for the clinical application of the PTT.[45]

Photothermal Stability and Photothermal Conversion Efficiency. The stability of PTAs is an essential factor in measuring PTT effectiveness. As shown in Figure 3A, FPI NPs were irradiated (793 nm, 0.33 W/cm^2) and then cooled for 5 cycles. There was no apparent degradation after 5 cycles, which revealed FPI NPs were sufficiently stable during PTT (Figure 3C). The stability of FPI NPs was further explored, which used UV−vis spectra before and after laser radiation, as shown in Figure S2B. The UV−vis spectrum of FPI NPs after laser irradiation (10 min) was observed an optical intensity slightly decreased as compared to the curve without laser radiation. This phenomenon was caused by the slight photothermal instability of ICG.[36] The recycling heating−cooling curve inferred the photothermal reversibility and recycling performance of FPI NPs. The photothermal conversion efficiency of bare Fe_3O_4 and FPI NPs were tested to conclude PTAs' ability to convert light to heat energy. As illustrated in Figure 3B,D, the temperature change of FPI NPs and bare Fe_3O_4 in an aqueous dispersion (concentration of 100 μg/mL) were recorded, respectively.

During laser irradiation, the temperature of FPI NPs solutions rapidly reached 53.3 °C and down to room temperature without laser radiation. Through laser radiation, FPI NPs exhibited a fast response. The photothermal conversion efficiency of FPI NPs and bare Fe_3O_4 are shown in Figure 3D, respectively. Compared with bare Fe_3O_4 (η = 22.18%), the FPI NPs showed higher photothermal conversion efficiency (η = 35.21%). According to previous work,[46] the Fe_3O_4 coated by the PDA has a better performance in photothermal efficiency compared with pure Fe_3O_4. The improved photothermal conversion efficiency of FPI NPs revealed that the modification of FPI NPs was helpful in enhancing the PTT properties.

Cytotoxicity Assay and Cellular Uptake. The NIR fluorescence property of FPI NPs and Fe_3O_4 NPs were analyzed. As shown in Figure 4A, the FPI NPs (right) showed the fluorescence intensity with the CLSM to confirm the NIR fluorescence property. In contrast, there was no fluorescence in Fe_3O_4 NPs (left). To verify the cytotoxicity of FPI NPs, the viability of HeLa cells incubated with samples was studied

https://doi.org/10.1021/acsomega.3c01374
ACS Omega 2023, 8, 21793−21801

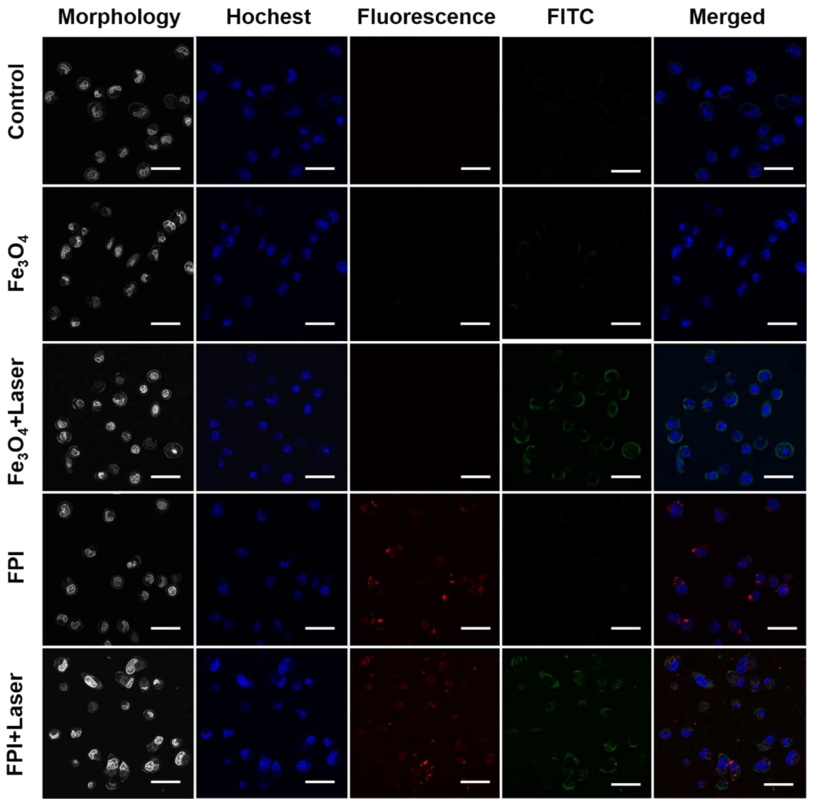

Figure 5. CLSM images of the samples (40 μg/mL) in HeLa cells treated with different conditions (DMEM, Fe_3O_4, FPI, Fe_3O_4 and laser, and FPI and laser) (scale bar = 500 μm).

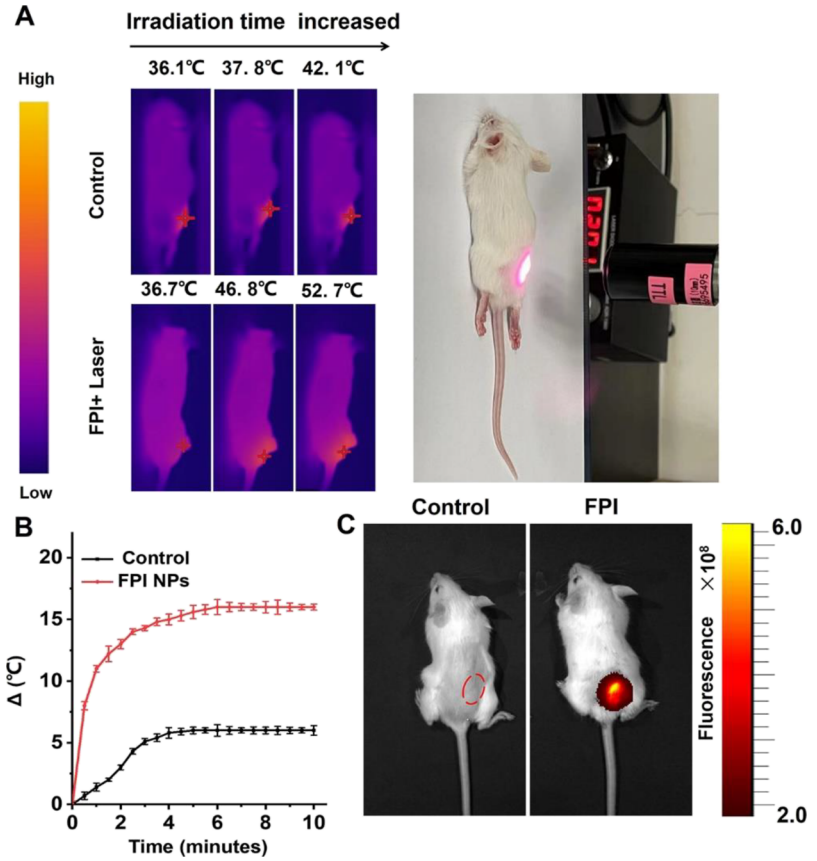

Figure 6. Under 793 nm NIR light irradiation (A) infrared thermal images of the mice treated with PBS and FPI NPs. (B) Temperature change curve of the subcutaneous injection site. (C) NIR fluorescence images of mice through the subcutaneous injection with PBS and FPI NPs at 2 h.

https://doi.org/10.1021/acsomega.3c01374
ACS Omega 2023, 8, 21793−21801

using the CCK-8 method without laser irradiation. With the increased sample concentrations, cell viability showed a significant downward trend (Figure 4B). The cell viability of the Fe_3O_4 and FPI NPs groups were 85.7 and 94.5% at a concentration of 40 μg/mL, respectively. Even at 100 μg/mL, the cell viability of the FPI NPs group could still reach 86.1%. The viability of HeLa cells incubated with samples was further studied. The flow cytometric analysis was performed to verify the cytotoxicity of samples, as shown in Figure 4D. Therefore, the results showed that FPI NPs had low cytotoxicity and the dark toxicity of FPI NPs to HeLa cells is lower than that of Fe_3O_4 NPs. As shown in Figure 4C, only laser irradiation did not reduce the cell viability, indicating that the laser alone would not damage HeLa cells. After 10 min of laser irradiation at 0.33 W/cm^2, the cell viability significantly decreased with the increase in concentration, and the cell viability of the FPI NPs group decreased more obviously than the Fe_3O_4 NPs group. When the concentration of FPI NPs reached 100 μg/mL, the cell viability decreased to 38.9%. The results showed that FPI NPs have strong phototoxicity to HeLa cells.

In Vitro Evaluation of the PTT Effect. To determine the ability of FPI NPs to pass through the cell membrane and be taken up by cells, HeLa cell uptake in vitro was observed with CLSM. The nuclei of HeLa cells were stained with Hoechst 33342, which showed fluorescence in the blue channel (control group), while FPI NPs showed fluorescence in the red channel (λ_{em} = 800−1000 nm, λ_{ex} = 640 nm) for the existing ICG. The results are shown in Figures 5 and S4 under a range of different experimental conditions (control, HeLa cells treated with DMEM, Fe_3O_4, FPI, Fe_3O_4 and laser, and FPI and laser. Notably, FPI NPs were taken up by the cells and distributed in the cytoplasm with emission in the red channel. In contrast, the Fe_3O_4 did not produce emission in the red channel, but its ability to enter cells was demonstrated by bright-field photos (Figure 4E. It has been demonstrated that FPI NPs can enter HeLa cells, achieve localization, and label HeLa cells (Figure 4F). Additionally, the result reflected that FPI NPs could be used for NIR fluorescence imaging-guided PTT treatment. Furthermore, a large amount of fluorescence was detected in the green channel in HeLa cells when treated with both laser and FPI, in which the therapeutic efficiency of the FPI on cells reached 81.81%. In Figure 5, the data showed that laser treatment promotes the cellular uptake of NPs.[47,48] Above all, the results indicated the effectiveness of FPI in treating cancer cells.

In Vivo PTT Effect and Fluorescence Property. Under 793 nm NIR light irradiation, the infrared thermal images of mice were reflected in vivo PTT effects of FPI NPs. Under 793 nm NIR light irradiation, the mice were irradiated for 10 min. Compared with control group 1, the temperature of the subcutaneous injection site increased from 36.7 to 52.7 °C for group 2, which was subcutaneously injected with FPI NPs (Figure 6A,B). Its final temperature exceeded the temperature required for thermal apoptosis of tumor cells (42 °C),[49] which verified the excellent cancer ablation efficiency of FPI NPs. In vivo NIR fluorescence images at 2 h were performed to analyze the fluorescence property of the sample. As for the control group, there was no fluorescence intensity in mice (Figure 6C). The fluorescence intensity of FPI NPs was displayed, and the results showed that FPI NPs had good fluorescence property.

CONCLUSIONS

The FPI NPs were formed by NIR excitable ICG via encapsulation of polydopamine (PDA) based on magnetic Fe_3O_4. The FPI nanoplatform showed good chemical stability in the aqueous solution. The FPI NPs displayed improved photothermal performance compared to the three components (Fe_3O_4, PDA, and ICG) in the spherical structure. With a safe power density (0.33 W/cm^2) of 793 nm laser irradiation, FPI NPs could generate hyperthermia of 54.1 °C for an irradiation time of 10 min. During this period, FPI NPs are sufficiently stable. Additionally, the in vitro photothermal conversion efficiency was measured to be 35.21%. Furthermore, the cytotoxicity test treated with FPI NPs on HeLa cells had a survival rate larger than 90%, confirming low cytotoxicity. With laser irradiation, the therapeutic efficiency of the FPI on cells reached 81.81%. Therefore, the FPI NPs with highly effective therapeutic effects have proven to provide a powerful tool for cancer therapy.

ASSOCIATED CONTENT

Supporting Information

The Supporting Information is available free of charge at https://pubs.acs.org/doi/10.1021/acsomega.3c01374.

The relevant materials and reagents used in the whole experiment, information about the relevant instrument involved in the work, and the statistical analysis refer to this work; T2-weighted MR images; UV−vis curve of Fe_3O_4 and FPI NPs; fluorescence quantitative analysis in CLSM images of the samples (40 μg/mL) in HeLa cells treated with different conditions (DMEM, Fe_3O_4, FPI, Fe_3O_4 and laser, and FPI and laser); the stability of FPI NPs at pre-set time points (0, 12, 24 and 36 h) (PDF)

AUTHOR INFORMATION

Corresponding Authors

Nuernisha Alifu − *State Key Laboratory of Pathogenesis, Prevention, and Treatment of High Incidence Diseases in Central Asia/School of Medical Engineering and Technology, Xinjiang Medical University, Urumqi 830054, China*; Email: nens_xjmu@126.com

Ke Sun − *School of Materials and Energy, University of Electronic Science and Technology of China, Chengdu 610054, China*; Email: ksun@uestc.edu.cn

Authors

Linxue Zhang − *State Key Laboratory of Pathogenesis, Prevention, and Treatment of High Incidence Diseases in Central Asia/School of Medical Engineering and Technology, Xinjiang Medical University, Urumqi 830054, China; School of Materials and Energy, University of Electronic Science and Technology of China, Chengdu 610054, China;* orcid.org/0000-0003-3452-2213

Gulinigaer Alimu − *State Key Laboratory of Pathogenesis, Prevention, and Treatment of High Incidence Diseases in Central Asia/School of Medical Engineering and Technology, Xinjiang Medical University, Urumqi 830054, China*

Zhong Du − *State Key Laboratory of Pathogenesis, Prevention, and Treatment of High Incidence Diseases in Central Asia/Department of Gynecology, The First Affiliated Hospital of Xinjiang Medical University, Urumqi 830054, China*

Ting Yan − *State Key Laboratory of Pathogenesis, Prevention, and Treatment of High Incidence Diseases in Central Asia/*

https://doi.org/10.1021/acsomega.3c01374
ACS Omega 2023, 8, 21793−21801

School of Medical Engineering and Technology, Xinjiang Medical University, Urumqi 830054, China

Hui Li − *State Key Laboratory of Pathogenesis, Prevention, and Treatment of High Incidence Diseases in Central Asia/School of Medical Engineering and Technology, Xinjiang Medical University, Urumqi 830054, China*

Rong Ma − *State Key Laboratory of Pathogenesis, Prevention, and Treatment of High Incidence Diseases in Central Asia/Department of Gynecology, The First Affiliated Hospital of Xinjiang Medical University, Urumqi 830054, China*

Zhongwen Lan − *School of Materials and Energy, University of Electronic Science and Technology of China, Chengdu 610054, China*

Zhong Yu − *School of Materials and Energy, University of Electronic Science and Technology of China, Chengdu 610054, China*

Complete contact information is available at: https://pubs.acs.org/10.1021/acsomega.3c01374

Author Contributions

[#]L.Z. and G.A. contributed equally to this work.

Funding

This work was financially supported by the Natural Science Foundation of Xinjiang Uygur Autonomous Region Regional Program (2021D01C29 and 2022E02130), the National Natural Science Foundation of China (No. 82202220 and No.62035011), the Fundamental Research Funds for the Central Universities and State Key Laboratory of Pathogenesis, Prevention, and Treatment of High Incidence Diseases in Central Asia Fund (No. SKL-HIDCA-2022-3), Xinjiang Medical University, the State Key Laboratory of Central Asian High Incidence Causes and Prevention (No. xyd2021Y005), and Xinjiang Uygur Autonomous Region University Scientific Research Program (XJEDU2022P058).

Notes

The authors declare no competing financial interest.

■ ACKNOWLEDGMENTS

We are grateful for the valuable suggestion of Dr. Lei fang. Natural Science Foundation of Xinjiang Uygur Autonomous Region. Linxue, Zhang (No. 2021D01C293). Nuernisha Alifu was financially supported by Xinjiang Uygur Autonomous Region (No. 2022E02130), the National Natural Science Foundation of China (No. 82202220 and No.62035011), the Fundamental Research Funds for the Central Universities and State Key Laboratory of Pathogenesis, Prevention and Treatment of High Incidence Diseases in Central Asia Fund (No. SKL-HIDCA-2022-3), Xinjiang Medical University, the State Key Laboratory of Central Asian High Incidence Causes and Prevention (No. xyd2021Y005), and Xinjiang Uygur Autonomous Region University Scientific Research Program (XJEDU2022P058).

■ REFERENCES

(1) Alifu, N.; Ma, R.; Zhu, L. J.; Du, Z.; Chen, S.; Yan, T.; Alimu, G.; Zhang, L. X.; Zhang, X. L. A Novel TMTP1-modified theranostic nanoplatform for targeted in vivo NIR-II fluorescence imaging-guided chemotherapy of cervical cancer. *J. Mater. Chem. B* **2022**, *10*, 506−517.

(2) Zhu, L. J.; Chen, J. J.; Yan, T.; Alimu, G.; Zhang, X. L.; Chen, S.; Aimaiti, M.; Ma, R.; Alifu, N. Near-infrared emissive polymer-coated IR-820 nanoparticlesassisted photothermal therapy for cervical cancer cells. *J. Biophotonics.* **2021**, *14*, No. e202100117.

(3) Shrestha, A. D.; Neupane, D.; Vedsted, P.; Kallestrup, P. Cervical cancer prevalence, incidence and mortality in low and middle income countries: a systematic review. *Asian Pac. J. Cancer Prev.* **2018**, *19*, 319−324.

(4) Asami, Y.; Yutaka, U.; Mamoru, K.; Yusuke, T.; Sayaka, I.; Shinya, M.; Eiji, K.; Toshitaka, M.; Isao, M.; Keisuke, F.; Yuri, I.; Tomio, N.; Tadashi, K. Epidemiologic and clinical analysis of cervical cancer using data from the population-based Osaka cancer registry. *Cancer Res.* **2019**, *79*, 1252−1259.

(5) Liu, S.; Pan, X.; Liu, H. Two-dimensional nanomaterials for photothermal therapy. *Angew. Chem. Int. Ed.* **2020**, *132*, 5943−5953.

(6) Zhou, H.; Zeng, X.; Li, A. G.; Zhou, W. Y.; Tang, L.; Hu, W. B.; Fan, Q. L.; Meng, X. L.; Deng, H.; Duan, L.; Li, Y. Q.; Deng, Z. X.; Hong, X.; Xiao, Y. L. Upconversion NIR-II fluorophores for mitochondria-targeted cancer imaging and photothermal therapy. *Nat. Commun.* **2020**, *11*, 6183−6192.

(7) Liu, X. Y.; Zhang, Y.; Wu, H.; Tang, J. W.; Zhou, J.; Zhao, J. L.; Wang, S. G. A conductive gelatin methacrylamide hydrogel for synergistic therapy of osteosarcoma and potential bone regeneration. *Int. J. Biol. Macromol.* **2023**, *228*, 111−122.

(8) Zhang, L. X.; Chen, S.; Ma, R.; Zhu, L. J.; Yan, T.; Alimu, G.; Du, Z.; Alifu, N.; Zhang, X. L. NIR-excitable PEG-modified Au nanorods for photothermal therapy of cervical cancer. *ACS Appl. Nano Mater.* **2021**, *4*, 13060−13070.

(9) Du, Z.; Ma, R.; Chen, S.; Fan, H. M.; Heng, Y. Q.; Yan, T.; Alimu, G.; Zhu, L. J.; Zhang, X. L.; Alifu, N. A highly efficient polydopamine encapsulated clinical ICG theranostic nanoplatform for enhanced photothermal therapy of cervical cancer. *Nanoscale Adv.* **2022**, *4*, 4016−4024.

(10) Li, X.; Hetjens, L.; Wolter, N.; Li, H. L.; Shi, X. Y.; Pich, A. Charge-reversible and biodegradable chitosan-based microgels for lysozyme-triggered release of vancomycin. *J. Adv. Res.* **2023**, *43*, 87−96.

(11) Lu, Y.; Luo, Q. L.; Jia, X. B.; Tam, J. P.; Yang, H.; Shen, Y. P.; Li, X. Multidisciplinary strategies to enhance therapeutic effects of flavonoids from Epimedii Folium: Integration of herbal medicine, enzyme engineering, and nanotechnology. *J. Pharm. Anal.* **2023**, *13*, 239.

(12) Wang, Y. F.; Meng, H. M.; Li, Z. Near-infrared inorganic nanomaterial-based nanosystems for photothermal therapy. *Nanoscale* **2021**, *13*, 8751−8772.

(13) Zhao, T. Y.; Cao, Y. N.; Sun, J.; Zhou, Q.; Liang, X. J.; Zhang, S. B. Temperature-sensitive lipid-coated carbon nanotubes for synergistic photothermal therapy and gene therapy. *ACS Nano* **2021**, *15*, 6517−6529.

(14) Qi, J.; Alifu, N.; Zebibula, A.; Wei, P.; Tang, Z. Highly stable and bright AIE dots for NIR-II deciphering of living rats. *NanoToday* **2020**, *34*, 100893−100993.

(15) Liu, B.; Li, C. X.; Chen, G. Y.; Liu, B.; Deng, X.; Wei, Y.; Xia, J.; Ma, P.; Lin, J. Synthesis and optimization of MoS_2@Fe_3O_4-ICG/Pt (IV) nanoflowers for MR/IR/PA bioimaging and combined PTT/PDT/chemotherapy triggered by 808 nm laser. *Adv. Sci.* **2017**, *4*, 1600540−1600552.

(16) Fan, H. M.; Chen, S.; Du, Z.; Yan, T.; Alimu, G.; Zhu, L. J.; Ma, R.; Alifu, N.; Zhang, X. L. New indocyanine green therapeutic fluorescence nanoprobes assisted high-efficient photothermal therapy for cervical cancer. *Dyes Pigm.* **2022**, *200*, 110174−110183.

(17) Li, X.; Lu, S. Y.; Xiong, Z. G.; Hu, Y.; Shen, M. W.; Shi, X. Y. Light-addressable nanoclusters of ultrasmall iron oxide nanoparticles for enhanced and dynamic magnetic resonance imaging of arthritis. *Adv. Sci.* **2019**, *6*, 1901800−1901812.

(18) Zhang, F.; Lu, G. H.; Wu, M. Y.; Cheng, Q. Y.; Yu, Y. K.; Tang, J.; Mei, L. Magnetic nanoparticles coated with polyphenols for spatio-temporally controlled cancer photothermal/immunotherapy. *J. Controlled Release* **2020**, *326*, 131−139.

(19) Chu, M. Q.; Shao, Y. X.; Peng, J. L.; Shi, D. L. Near-infrared laser light mediated cancer therapy by photothermal effect of Fe_3O_4 magnetic nanoparticles. *Biomaterials* **2013**, *34*, 4078−4088.

(20) Lin, L. S.; Cong, Z. X.; Cao, J. B.; Ke, K. M.; Peng, Q. L.; Gao, J. H.; Chen, X. Y. Multifunctional Fe_3O_4@Polydopamine core-shell nanocomposites for intracellular mRNA detection and imaging-guided photothermal therapy. *ACS Nano* **2014**, *8*, 3876−3883.
(21) Li, J. C.; Sun, W. J.; Shen, M. Y.; Zhang, G. X.; Shi, X. Y. Hyaluronic acid-modified Fe_3O_4@Au core/shell nanostars for multimodal imaging and photothermal therapy of tumors. *Biomaterials* **2015**, *38*, 10−21.
(22) Luo, K. Y.; Zhao, J. L.; Jia, C. Z.; Chen, Y. K.; Zhang, Z. L.; Zhang, J.; Huang, M. X.; Wang, S. G. Integration of Fe_3O_4 with Bi_2S_3 for multi-modality tumor theranostics. *ACS Appl. Mater. Interfaces* **2020**, *12*, 22650−22660.
(23) Wang, Y. D.; Pang, X. J.; Wang, J. P.; Tan, F. P.; Li, J.; Li, N. Magnetically-targeted and near infrared fluorescence/magnetic resonance/photoacoustic imaging-guided combinational anti-tumor phototherapy based on polydopamine-capped magnetic Prussian blue nanoparticles. *J. Mater. Chem. B* **2018**, *6*, 2460−2473.
(24) Zhou, Y. L.; Zhou, J.; Wang, F.; Yang, H. H. Polydopamine-based functional composite particles for tumor cell targeting and dual-mode cellular imaging. *Talanta* **2018**, *181*, 248−257.
(25) Zhang, Y.; Zhu, C. P.; Zhang, Z. R.; Zhao, J. L.; Yuan, Y. K.; Wang, S. G. Oxidation triggered formation of polydopamine-modified carboxymethyl cellulose hydrogel for anti-recurrence of tumor. *Colloids Surf., B* **2021**, *207*, 112025−112033.
(26) Nurunnabi, K. P.; Nafiujjaman, V. R.; Haseeb, A. K.; Feng, X. L.; Lee, Y. K. Bioapplication of graphene oxide derivatives: drug/gene delivery, imaging, polymeric modification, toxicology, therapeutics and challenges. *RSC Adv.* **2015**, *5*, 42141−42161.
(27) Li, N.; Li, T. T.; Hu, C.; Lei, X.; Zuo, Y. M.; Han, H. Targeted near-infrared fluorescent turn-on nanoprobe for activatable imaging and effective phototherapy of cancer cells. *ACS Appl. Mater. Interfaces* **2016**, *8*, 15013−15023.
(28) Hu, D. H.; Liu, C. B.; Song, L.; Cui, H. D.; Gao, G. H.; Liu, P.; Sheng, Z. H.; Cai, L. Indocyanine green-loaded polydopamine−iron ions coordination nanoparticles for photoacoustic/magnetic resonance dual-modal imaging-guided cancer photothermal therapy. *Nanoscale* **2016**, *8*, 17150−17158.
(29) Hu, D. H.; Zhang, J. J.; Gao, G. H.; Sheng, Z. H.; Cui, H. D.; Cai, L. Indocyanine green-loaded polydopamine-reduced graphene oxide nanocomposites with amplifying photoacoustic and photothermal effects for cancer theranostics. *Theranostics* **2016**, *6*, 1043−1052.
(30) Huang, X. Q.; Wu, J. R.; He, M. Y.; Hou, X. Y.; Wang, Y.; Chen, Y. Combined cancer chemo-photodynamic and photothermal therapy based on ICG/PDA/TPZ-loaded nanoparticles. *Mol. Pharmaceutics* **2019**, *16*, 2172−2183.
(31) Liu, F.; He, X.; Lei, Z.; Liu, L.; Zhang, J.; You, H.; Zhang, H.; Wang, Z. Facile preparation of doxorubicin-loaded upconversion@polydopamine nanoplatforms for simultaneous in vivo multimodality imaging and chemophotothermal synergistic therapy. *Adv. Healthcare Mater.* **2015**, *4*, 559−568.
(32) Dong, Z. L.; Gong, H.; Gao, M.; Zhu, W. W.; Sun, X. Q.; Liu, Z. Polydopamine nanoparticles as a versatile molecular loading platform to enable imaging-guided cancer combination therapy. *Theranostics* **2016**, *6*, 1031−1042.
(33) Liu, B.; Li, C. X.; Xing, B. G.; Yang, P. P.; Lin, J. Multifunctional UCNPs@PDA-ICG nanocomposites for upconversion imaging and combined photothermal/photodynamic therapy with enhanced antitumor efficacy. *J. Mater. Chem. B* **2016**, *4*, 4884−4894.
(34) Damian, M.; Bartosz, F.; Emerson, C.; Stefan, J.; Radosław, M. NDs@PDA@ICG conjugates for photothermal therapy of glioblastoma multiforme. *Biomimetics* **2019**, *4*, 3.
(35) Zhang, T.; Chai, H.; Meng, F. Y.; Guo, Z. Z.; Jiang, Y.; Miao, P. DNA-functionalized porous Fe_3O_4 nanoparticles for the construction of self-powered miRNA biosensor with target recycling amplification. *ACS Appl. Mater. Interfaces* **2018**, *10*, 36796−36804.
(36) Xue, P.; Hou, M. M.; Zhang, L.; Xu, Z. G.; Kang, Y. J. Calcium-carbonate packaging magnetic polydopamine nanoparticles loaded with indocyanine green for near-infrared induced photothermal/photodynamic therapy. *Acta Biomater.* **2018**, *81*, 242−255.
(37) Natanael, F.; Carolina, F. R.; André, F. M.; Ilídio, J. C. Overview of the application of inorganic nanomaterials in cancer photothermal therapy. *Biomater. Sci.* **2020**, *8*, 2990−3020.
(38) Altinoglu, E. I.; Russin, T. J.; Kaiser, J. M.; Barth, B. M.; Eklund, P. C.; Kester, M.; Adair, J. H. Near-infrared emitting fluorophore-doped calcium phosphate nanoparticles for in vivo imaging of human breast cancer. *ACS Nano* **2008**, *2*, 2075−2084.
(39) Patel, R. H.; Wadajkar, A. S.; Patel, N. L.; Kavuri, V. C.; Nguyen, K. T.; Liu, H. L. Multifunctionality of indocyanine green-loaded biodegradable nanoparticles for enhanced optical imaging and hyperthermia intervention of cancer. *J. Biomed. Opt.* **2012**, *17*, No. 046003.
(40) Wang, L. Y.; Hui, L. F.; Su, W. Y. Superhydrophobic modification of nanocellulose based on an octadecylamine/dopamine system. *Carbohydr. Polym.* **2022**, *275*, 118710−118722.
(41) Li, X.; Xing, L. X.; Zheng, K. L.; Shen, M. W.; Shi, X. Y. Formation of gold nanostar-coated hollow mesoporous silica for tumor multimodality imaging and photothermal therapy. *ACS Appl. Mater. Interfaces* **2017**, *9*, 5817−5827.
(42) Mostafa, Y.; Kamyar, S.; Ziba, H.; Sin, T.; Umi, N.; Roshafima, R. Green synthesis of Fe_3O_4 nanoparticles for hyperthermia, magnetic resonance imaging and 5-fluorouracil carrier in potential colorectal cancer treatment. *Res. Chem. Intermed.* **2021**, *47*, 1789−1808.
(43) Karunanidhi, G.; Vellingiri, Y.; Raju, V. Emerging indocyanine green-integrated nanocarriers for multimodal cancer therapy: a review. *Nanoscale Adv.* **2021**, *3*, 3332−3352.
(44) Du, B. J.; Liu, J. H.; Ding, G. Y.; Han, X.; Li, D.; Wang, E.; Wang, J. Positively charged graphene/Fe_3O_4/polyethylenimine with enhanced drug loading and cellular uptake for magnetic resonance imaging and magnet-responsive cancer therapy. *Nano Res.* **2017**, *10*, 2280−2295.
(45) Chang, M. Y.; Hou, Z. Y.; Wang, M.; Li, F.; Liu, D.; Peng, T. L.; Li, C. X.; Lin, J. Single-atom Pd nanozyme for ferroptosis-boosted mild-temperature photothermal therapy. *Angew. Chem. Int. Ed.* **2021**, *60*, 12971−12979.
(46) Wang, Z.; Wang, G.; Kang, T. T.; Liu, S. W.; Liu, Y. $BiVO_4$/Fe_3O_4@polydopamine superparticles for tumor multimodal imaging and synergistic therapy. *J. Nanobiotechnol.* **2021**, *19*, 90.
(47) Li, X.; Kong, L. D.; Hu, W.; Pich, A.; Shi, X. Y.; Wang, X. P.; Xing, L. X. Safe and efficient 2D molybdenum disulfide platform for cooperative imaging-guided photothermal-selective chemotherapy. *J. Adv. Res.* **2022**, *37*, 255−266.
(48) Li, X.; Sun, H. T.; Li, H. L.; Hu, C. L.; Luo, Y.; Shi, X. Y.; Pich, A. Multi-responsive biodegradable cationic nanogels for highly efficient treatment of tumors. *Adv. Funct. Mater.* **2021**, *31*, 2100227−2100241.
(49) Chu, Y. J.; Xu, X. Q.; Wang, Y. P. Ultradeep photothermal therapy strategies. *J. Phys. Chem. Lett.* **2022**, *13*, 9564−9572.

https://doi.org/10.1021/acsomega.3c01374
ACS Omega 2023, 8, 21793−21801